Proceedings World Geothermal Congress 2023
Beijing, China, April 17 – 21, 2023

Ground Surface Temperature Monitoring Data Interpretation and Implications for Subsurface Heat Flux in Southern Mount Meager, Western Canada

Zhuoheng Chen, Stephen E. Grasby, Wanju Yuan and Xiaojun Liu

3303 33rd Street NW. Calgary, T2L 2A7, Alberta, Canada

Zhuoheng.chen@nrcan-rncan.gc.ca

Keywords: Ground surface temperature monitoring; Snow curtaining; Geothermal heat flux; Machine learning; Geophysics guided interpretation

ABSTRACT

Previous studies showed that ground surface temperature (GST) monitoring data contain information indicative of subsurface geothermal flux in the Mount Meager Volcanic Complex (MMVC) of western Canada. This paper reviews the statistical methods for GST feature extraction, characterization, and environmental impact suppression. The resulting ground surface anomalies from GST data were examined against the geothermal drilling results and an inverted resistivity model from AMT data, in conjunction with areal infrared thermal images of the same area to investigate possible links between the GST anomalies and subsurface heat flux. The temporal variation of GST time series recorded at 22 stations across the study area is divided into three segments: pre- snow curtain (Pre-SC), snow curtain (SC) and post-snow curtain (post-SC) for the convenience of data analysis. The intensity of daily GST variation of the recorded GST time series in the snow free seasons shows predominantly seasonal and daily air temperature fluctuations in responding to heat energy from solar radiation and climate forcing with clear environmental footprints and complicated by soil properties. During the snow curtain period, all GST records leveled off, staying almost constant around 0 °C as the solar radiation has been greatly reduced by effective insolation from thick winter snow. Subtle differences among GST time series at different stations may reflect the spatial variation of the subsurface heat flux. Comparison with subsurface temperature data and groundwater discharge, the measured mean GST (SC) and duration of the SC show a close spatial affinity with subsurface heat flow and shallow ground water circulation revealed by drilling results and warm spring swarms along the margin of the volcanic complex and is consistent with the spatial distribution of low resistivity zones of the inverted resistivity model from AMT data.

1. INTRODUCTION

The feasibility of employing miniature temperature loggers for revealing geothermal heat flux related GST anomalies has been tested in southern Mount Meager, an identified geothermal prospect, in British Columbia, Canada (Chen et al., 2023). Preliminary analysis of the data, collected from 22 GST stations in the first year in the conceptual case study suggested that the GST monitoring data contains useful information, indicative of subsurface heat flow anomalies (Chen et al., 2023). The spatial coincidence between the GST anomalies and estimated subsurface high heat flow was used as evidence to argue for the linkage for the two. However, the intrinsic relationship and the linkage remain unexplained.

Previous subsurface drilling and various geophysical and geological studies have revealed the characteristics and geothermal resource potential and delineated the geothermal anomalies in the prospective area (e.g., Lewis and Souther, 1978; Fairbank, 1981a; GeothermEx Inc., 2004, 2009). A recently published resistivity model inverted from AMT data in the same area (Hormozzade Ghalati, et al., 2022) provides a 3D subsurface resistivity structure that could help interpret the link. This study uses available subsurface geological and geophysical survey data to constrain the GST data interpretation and the linkage between the identified anomalies and spatial variation of subsurface heat flux. We will review the statistical methods for the GST feature extraction, characterization, and environmental impact suppression first. The resulting ground surface anomalies from GST data are then analyzed along with the subsurface temperature data as well as the 3D resistivity model from AMT to establish the possible links between the GST anomalies and subsurface heat flux.

2. DATA AND METHODS

2.1 Data

Data were GST records of miniature temperature data loggers (HOBO Water Temp Pro v2) deployed in the study area from 2020-09-21 to 2021-08-16 with a programed temperature record for every 30 minutes. The HOBO sensor has temperature recording ranging from –40 °C to +70 °C in air with accuracy of ±0.2 °C and resolution of 0.02 °C. Twenty-two temperature data loggers were deployed in the south Meager geothermal prospect area and extended east-west to cover the area of known warm water seepages along the southeast segment of the Meager Creek (Lewis and Souther, 1978) (Fig. 1). For details of data collection and surface and topographic conditions, and quantitative measure for the impacts of vegetation on GST records, readers are referred to Chen et al. (2023). Table 1 summarizes the essential environmental variables and laboratory measured soil properties at each monitoring station.

Geological data and a geophysical inversion model (AMT resistivity model) used in this study are from literature and technical reports for the geothermal studies in the southern Mount Meager area (e.g., Lewis and Souther, 1978; Fairbank, 1981a; Fairbank engineering ltd, 2002; GeothermEx Inc., 2004, 2009; Hormozzade Ghalati, et al., 2022).

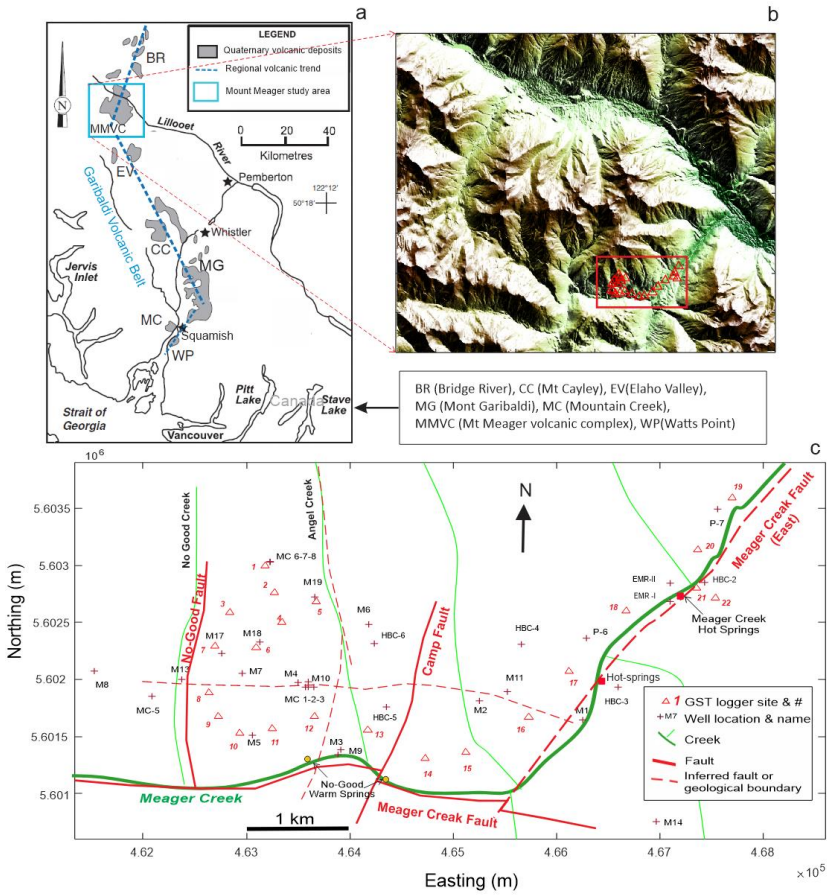

Figure 1: Location map showing the regional geological settings (a), geographic characteristics (digital elevation map, b), and the study area with local geological features in c). The location of the study area is shown as red polygon in b). Figure 1a is modified from Stewart, et al., (2002).

Site #	Latitude	Longitude	Elevation (m)	Burial Depth (cm)	Shadiness Index	sample soil Miosture (%)	Soil density (g/cm^3)	Soil thermal conductivity (W/m-k)	Thermal diffusivity (mm^2/s)
1	50.57770	123.51999	1386	2	0.2	31	1.31	0.444	0.196
2	50.57559	123.51872	1283	1	0.05	22	1.46	0.407	0.199
3	50.57401	123.52480	1178	2	0.1	18	1.48	0.402	0.198
4	50.57323	123.51769	1105	5	0.7	25	1.55	0.476	0.198
5	50.57492	123.51299	1117	4	0.1	38	1.33	0.451	0.198
6	50.57127	123.52118	1044	5	0.4	24.5	1.46	0.361	0.197
7	50.57137	123.52683	982	4	0.5	25	1.62	0.470	0.202
8	50.56766	123.52757	907	2	0.3	27.4	1.55	0.425	0.204
9	50.56583	123.52627	882	5	0.5	25	1.68	0.547	0.199
10	50.56452	123.52334	839	3	0.6	24.3	1.49	0.544	0.200
11	50.56489	123.51889	809	3	0.8	28.4	1.03	0.385	0.200
12	50.56589	123.51313	784	3	0.6	45	1.42	0.463	0.197
13	50.56481	123.50587	776	6	0.5	25	1.15	0.299	0.198
14	50.56263	123.49802	747	2	0.6	30.4	1.27	0.454	0.198
15	50.56313	123.49245	744	4	0.8	24.8	1.49	0.540	0.197
16	50.56595	123.48388	727	3	0.7	22.5	1.54	0.542	0.203
17	50.56958	123.47843	739	6	0.6	24	1.50	0.514	0.210
18	50.57435	123.47069	693	4	0.8	23.5	1.55	0.625	0.204
19	50.58332	123.45629	562	2	0.6	25.5	1.32	0.447	0.199
20	50.57921	123.46095	571	3	0.4	23.1	1.52	0.524	0.199
21	50.57641	123.46147	570	7	0.9	17.3	1.17	0.310	0.198
22	50.57543	123.45848	593	4	0.95	21.3	1.34	0.327	0.199

Table 1. Basic information and environmental conditions of the monitory stations in this study.

2.2 Methods and Data Analyses

Hierarchical clustering analysis (HCA) and Principal component analysis (PCA) were applied to the recorded time series for clustering and feature extraction. The HCA seeks to build a hierarchy of clusters based on statistical similarities. Clusters are determined in such a way so that objects in the same cluster are similar, while objects in different clusters differ significantly in a statistical sense (Davis, 2002). The determined similarity hierarchies in the data are visualized using a dendrogram plot. The resulting clusters are projected on a map to display their spatial characteristics. HCA is a non-supervised method, and no training data is required. However, a non-supervised method results in an ordinal variable, whose geological meaning is subject to interpretation.

In this study, PCA was used to extract and separate features from GST time series dominated by daily and seasonal variations in solar radiation. PCA transforms the original data into a new coordinate system linearly so that each of the newly transformed PCs is orthogonal to the others. After the transformation, the first PC contains the most information in the original dataset, while the last has the least information. As such, the specific signal that is potentially related to geothermal heat flow can be separated from the GST time series and represented by one of the re-organized data (PCs) under the new coordinate system for data interpretation.

3. RESULTS

3.1 General characteristics of the GST time series

The time series of the monitoring data collected from the 22 stations are plotted in Figure 2, showing the general characteristics of the daily variation and seasonal fluctuation of GST. The recorded temperatures drop below 0 °C in the early winter but remain almost constant around 0 °C once the ground is covered with thick snow through the entire winter. Temperatures resume their daily cycles and seasonal fluctuation when the snow cover is melted. We call the period with almost constant GST around zero the snow curtain (SC) period in this study. For convenience of data analysis, the collected temperature-time series is divided into three segments: a) pre- snow curtain (Pre-SC) with temperature above or slightly below zero, b) snow curtain (SC) with stable temperatures around 0 °C, and c) post- snow curtain (Pst-SC) segment with large daily GST fluctuation (Fig. 2a). It is notable that the length (days) of the snow curtain period varies from less than 135 days (St. #21) to over 210 days (St. # 1). There is an abrupt change in temperature from SC to Pst-SC segments, but a gradual transition from Pre-SC to SC is common. The monitoring stations are about equally spaced, starting from the upper drilling platform at around 1300 m and gradually descending elevation southeastward to the bank of Meager Creek at <600 m. The GST time series in that order can be projected into time and space as a temperature mesh surface (Fig. 2b) to reveal their temporal change and spatial variation in the study area. The widest daily temperature variation occurred in the post-SC period among the stations located at the highest elevation (St. #1, 2 and 3), while Stations #16-18 along river valley display a moderate daily variation (Fig. 2b).

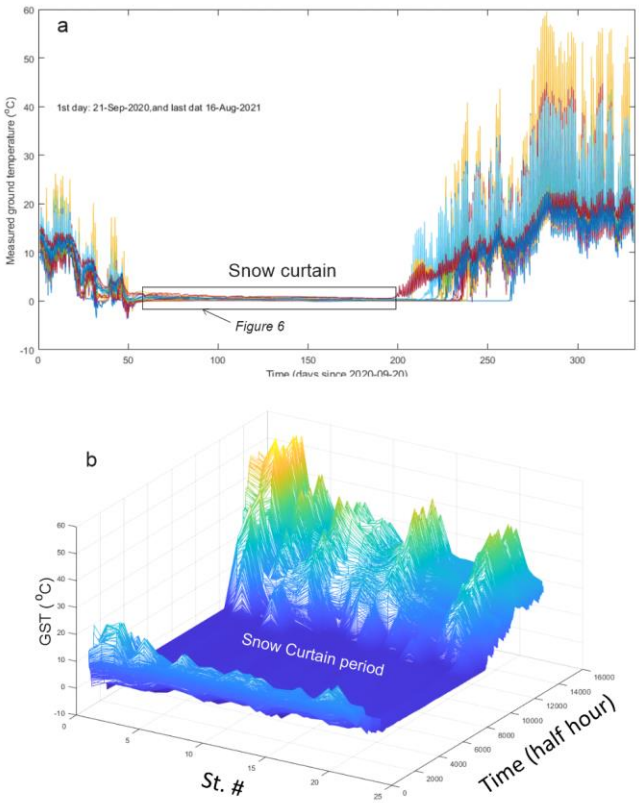

Figure 2: a) Recorded GST time series from 21-Sep-2020 to 16-Aug-2021 showing daily cycles and seasonal variations with a long flat temperature around zero in snow cover period, and b) Recorded GST time series plotted in a 3D view to emphasizing the variation among the stations.

3.2 Ground Surface Characterization

Statistical methods were applied to characterize ground surface settings by grouping stations with similar environmental condition, such as elevation, burial depth, vegetation effect, and soil properties (Table 1), such that their impacts can be quantitatively analyzed. The same methods are also applied to GST time series to assist geological interpretation that links potential GST anomalies, or particular feature groups, to subsurface geological features.

Table 2: Correlation coefficient matrix for statistics from GST time series and environmental variable. GST mean: mean for the full length records, and GST std: standard deviation of GST for the full length records.

	Days in Snow Curtain	GST mean in Snow Curtain	GST std in Snow Curtain	GST mean	GST std	Thermal consuctivity	Thermal diffusivity	Elevation	Burial depth	Soil moisture	Shadiness Index	Soil density
Days in SC	1	-0.661291	-0.12484	-0.54217	0.302572	0.315533598	-0.2106908	0.554355	-0.66761	0.514626	-0.39903	0.116199
GST mean in SC	-0.66129	1	0.351311	0.253638	-0.47148	-0.00790418	0.3474452	-0.64679	0.427991	-0.5198	0.5889801	-0.1707
GST std in SC	-0.12484	0.3513115	1	0.07053	-0.17893	0.206641915	0.4295731	-0.15222	0.158749	0.118434	-0.02676	-0.01645
GST mean	-0.54217	0.2536377	0.07053	1	0.562648	-0.20943795	0.1057609	-0.25521	-0.10444	-0.33026	-0.3176564	0.033692
GST std	0.302572	-0.471485	-0.17893	0.562648	1	-0.15677783	-0.2519896	0.465852	-0.61369	0.094579	-0.8502028	0.059137
Th consuctivity	0.315534	-0.007904	0.206642	-0.20944	-0.15678	1	0.381555	-0.08928	-0.16664	0.129161	0.0738943	0.664432
Th. diffusivity	-0.21069	0.3474452	0.429573	0.105761	-0.25199	0.381554974	1	-0.26216	0.147535	-0.16046	0.1563095	0.333005
elevation	0.554355	-0.646794	-0.15222	-0.25521	0.465852	-0.08927727	-0.2621618	1	-0.31711	0.280008	-0.7469152	0.159472
B depth	-0.66761	0.4279911	0.158749	-0.10444	-0.61369	-0.16664263	0.1475349	-0.31711	1	-0.22063	0.4595889	-0.07222
S moisture	0.514626	-0.519797	0.118434	-0.33026	0.094579	0.129161146	-0.1604611	0.280008	-0.22063	1	-0.2913218	-0.18833
SI	-0.39903	0.5889801	-0.02676	-0.31766	-0.8502	0.073894339	0.1563095	-0.74692	0.459589	-0.29132	1	-0.18757
S density	0.116199	-0.170703	-0.01645	0.033692	0.059137	0.664432425	0.3330048	0.159472	-0.07222	-0.18833	-0.1875685	1

3.2.1 Unsupervised classification from environmental variables

Chen et al. (2023) examined the impacts of environmental variables on GST records during the snow free period. Here we concentrate on the impacts during the snow curtain period and correlation analysis among the derivatives from GST records and environmental variables was conducted. Table 2 is a correlation coefficient matrix revealing the inter-relationship among those variables. The SI and burial depth show the highest negative correlations with GST std, whereas elevation and soil moisture have a positive impact on GST mean (SC). The burial depth and SI show negative correlation with the length of snow curtain, while elevation and soil moisture are positively correlated to the length of SC, and burial depth and Si show positive impacts on GST mean (SC). The correlation analysis indicates that the surface and environment conditions have considerable impacts on the recorded GST even in the snow curtain period.

The hierarchical clustering analysis was applied to the environmental variable summarized in Table 1 to provide a similarity hierarchical structure of the surface condition for the study area. The surface condition similarity measured by elevation, burial depth, vegetation cover and soil properties among the stations is depicted by the HCA, where stations with similar conditions are grouped into the same cluster. The dendrogram of HCA provides a hierarchical structure of the similarity relationship among the stations (Fig. 3a). In a statistic sense, the stations (#1 to 9) on the slope of the volcanic mountain and those along Meager Creek form two general clusters though each cluster can be further separated into a few smaller clusters that are closely connected in space (Figs. 3a and b).

The volcanic deposits covered terrain and basement outcrop area show more variabilities indicated by sub-clusters (A, B and C) at higher levels (larger statistic distances). Whereas those in the alluvial fans with thick overburden and dense vegetation along Meager Creek show more stable conditions (Fig. 3a). These can also be seen from the projected clustering map in space from the dendrogram (Fig. 3b).

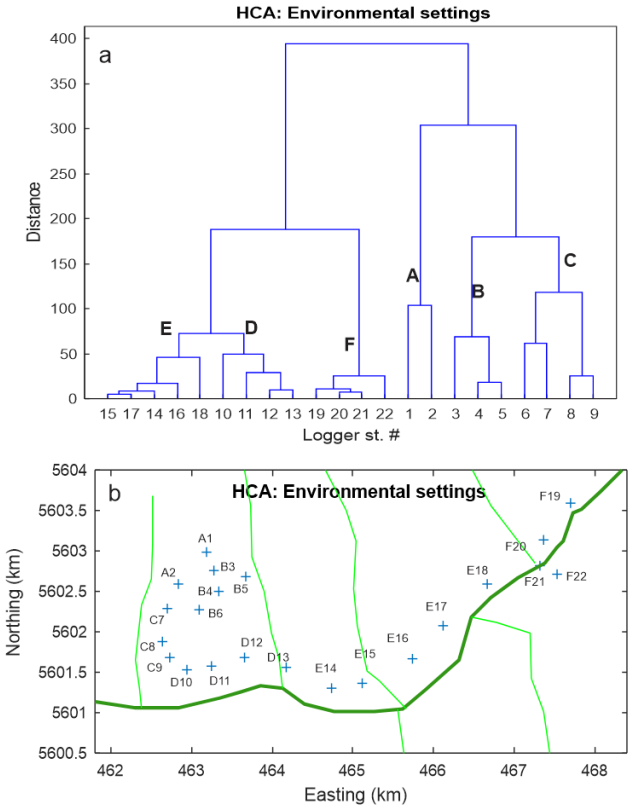

Figure 3: Clustering from environmental variables in Table 1. Dendrogram of HCA a), and map projection b) of the classification from the HCA for the environmental variables. Green: geographic reference of creek. Text code: letter indicating class and number is station. In the data interpretation class Cd is treated as class C for simplicity.

3.2.2 Feature extraction using Principal Component Analysis (PCA)

In order to further reveal the relationship between GST and environmental parameters, the 22 original GST time series are mathematically transformed into mutually independent principal components (PCs) by PCA. Among the PCs, the first PC accounts for over 94% of variance in the original 22 GST time series, while the next four PCs account for about 5% (Figure 4a). The bar charts (Figs. 4b-f) show relative contribution of the original GST recorded at different stations as the PCs. The PC-1 (Fig.4b) receives contributions from each of the 22 GST almost equally, reflecting predominantly the solar induced daily and seasonal fluctuations of GST (Fig. 5). For PC-2, GSTs from St. #1, 2, 3, and 5 at high altitude dominates the positive side and #12, 13, 17, 18, 20 and 21 stationed in low altitude the negative side (Figs. 4c), evidencing the impact of elevation (Fig. 5), while PC-3 contain mostly information from SI and burial depth as indicated from the correlation coefficients (Fig. 4d and Table 3), and PC-4 the soil moisture (Fig. 5 and Table 3). We can interpret the contribution of other PCs in the same way, that is, the longer the bar, the greater the contribution it makes, (Figs. 4e).

A correlation analysis of the loadings of first 10 PCs with environmental variables reveals the relationship between PCs and the environmental variables (Table 3). For example, PC-1 represents the general characteristics of the GST time series, and is negatively correlated with SI and burial depth, suggesting that high SI and deeper burial could pull down the GST and variation in GST in the daily cycle. PC-2 has a positive correlation with elevation, but a negative with burial depth, indicating that the elevation could increase the daily variation of the GST, while the burial depth does the opposite. A moderate negative correlation was observed between PC-4 and soil moisture. The environmental variable's effect on GST can be seen in the temporal domain (Fig. 5). For example, the SI and burial depth had more impact during the post SC (PC-1), burial and elevation in the SC and post-SC, while moisture effect is seen more in the transition period from SC to post-SC (PC-4 in Fig. 5).

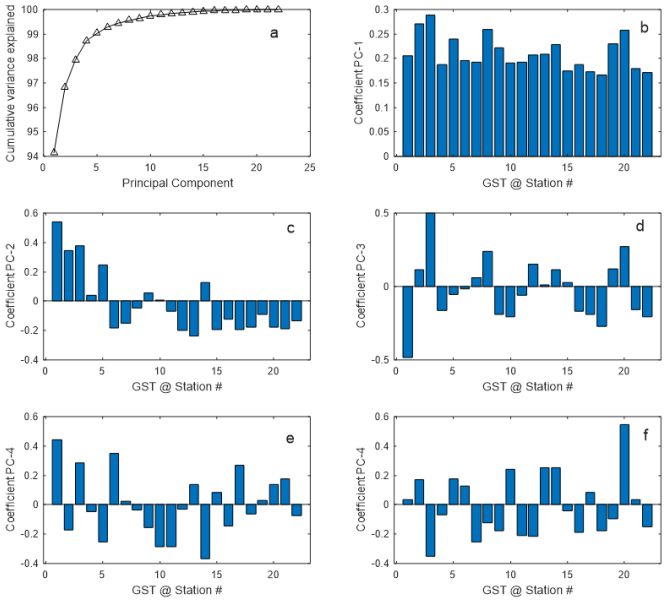

Figure 4: Results from PCA analysis. Information carried in the original GST time series a), Contributions from each GST time series to PC-1 b), PC-2 c), PC-3 d), PC-4 e) and PC-5 f).

Table 3. Correlation coefficient matrix of environmental variables and first 10 Principal Components from PCA.

	Thermal Conductivity	Thermal Diffusivity	Elevation	Depth	Moisture	SI	Density	PC1	PC2	PC3	PC4	PC5	PC6	PC7	PC8	PC9	PC10
T. Conductivity	1	0.38	-0.09	-0.17	0.13	0.07	0.66	-0.15	-0.04	-0.18	-0.23	-0.05	-0.2	-0.03	-0.19	-0.1	-0.14
T. Diffutivity	0.38	1	-0.26	0.15	-0.16	0.16	0.33	-0.22	-0.33	-0.12	-0.05	-0.15	0.17	-0.02	0	-0.25	0.21
Elevation	-0.09	-0.26	1	-0.32	0.28	-0.75	0.16	0.38	0.79	-0.03	0.18	-0.08	0.24	0.3	0	-0.01	0.27
Depth	-0.17	0.15	-0.32	1	-0.22	0.46	-0.07	-0.6	-0.56	-0.38	0.27	0.07	0.42	0.02	-0.13	0.22	-0.08
Moisture	0.13	-0.16	0.28	-0.22	1	-0.29	-0.19	0.08	0.26	-0.14	-0.32	0.17	-0.24	0.03	0.04	0.5	0.38
SI	0.07	0.16	-0.75	0.46	-0.29	1	-0.19	-0.81	-0.7	-0.38	-0.19	-0.22	-0.09	-0.2	0.11	-0.15	-0.29
Density	0.66	0.33	0.16	-0.07	-0.19	-0.19	1	0.09	-0.02	0.07	0.05	-0.18	0.03	0.26	-0.19	-0.14	0.1
PC1	-0.15	-0.22	0.38	-0.6	0.08	-0.81	0.09	1	0.55	0.73	-0.02	0.17	-0.04	0.13	-0.03	0.14	0.02
PC2	-0.04	-0.33	0.79	-0.56	0.26	-0.7	-0.02	0.55	1	-0.01	0	0	0	0	0	0	0
PC3	-0.18	-0.12	-0.03	-0.38	-0.14	-0.38	0.07	0.73	-0.01	1	0	0	0	0	0	0	0
PC4	-0.23	-0.05	0.18	0.27	-0.32	-0.19	0.05	-0.02	0	0	1	0	0	0	0	0	0
PC5	-0.05	-0.15	-0.08	0.07	0.17	-0.22	-0.18	0.17	0	0	0	1	0	0	0	0	0
PC6	-0.2	0.17	0.24	0.42	-0.24	-0.09	0.03	-0.04	0	0	0	0	1	0	0	0	0
PC7	-0.03	-0.02	0.3	0.02	0.03	-0.2	0.26	0.13	0	0	0	0	0	1	0	0	0
PC8	-0.19	0	0	-0.13	0.04	0.11	-0.19	-0.03	0	0	0	0	0	0	1	0	0
PC9	-0.1	-0.25	-0.01	0.22	0.5	-0.15	-0.14	0.14	0	0	0	0	0	0	0	1	0
PC10	-0.14	0.21	0.27	-0.08	0.38	-0.29	0.1	0.02	0	0	0	0	0	0	0	0	1

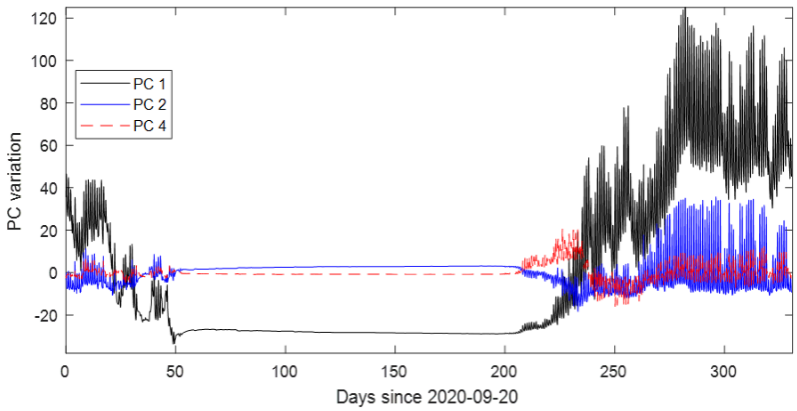

Figure 5: GST transformed principal components showing general characteristics of the GST time series represented by PC-1, which carries more than 94% of information in the original GST timeseries, and less information in PC-2 (about 2.5% variance), displaying the impacts predominantly from elevation, shadiness and burial depth, and PC-4 with more obvious impact from moisture.

3.3 GST anomaly mapping of snow curtain period

Although GSTs in the snow curtain period are relatively stable due to the insulation effect of thick snow, the subtle difference in GST variation may contain information indicative of variation of the subsurface heat flow. Figure 6a details observed GST variation in the SC period as a time series plot and a time-space mesh plot (Fig. 6b) to reveal the tempo-spatial trends of the data.

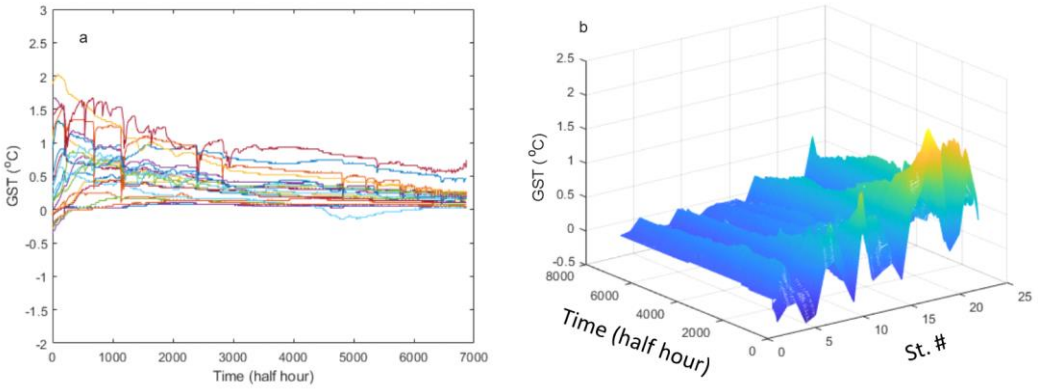

Figure 6: GST time series in the snow curtain period a), and the same time series shown in 3D mesh view to show the GST variations among the stations in snow curtain b).

Our previous study indicated that the environmental factors also exert similar impacts on the GST in the snow curtain period although the intensity is less (Chen et al., 2023). To eliminate the impacts on the recorded GST, a multivariate linear regression is applied to the GST data. Two indicators were used in the analysis, the mean GST in the SC period, and the number of days in the SC period. Here we use the residues of the two indicators from the regression models to delineate the GST anomalies (Chen et al., 2023). Statistically in a regression model, the square of correlation coefficient, r^2, is a statistic measure, representing the percentage of variation contributed from the independent variables to the dependent variable. The residues, defined as the difference between observed and model predicted, are the un-explained variations, presumably caused primarily by the ground heat flux. We chose the most relevant environmental variables (highly correlated with the indicators: elevation, SI, burial depth, thermal conductivity and soil moisture) as the independent variable in the regression. For the GST mean (SC), elevation, burial depth and soil moisture were included, while for the number of days, variables elevation, SI and soil moisture were used for the regression. For the mean GST model (SC), r^2=0.58, meaning that 58% of the variation in the mean GST in SC are from elevation, burial depth and soil moisture; while r^2 =0.77 for days in SC, the elevation, burial depth and soil moisture combined contribute more than half of the variation in days of SC.

The residuals of the models for GST mean (SC) and days of SC generated similar spatial patterns and depicted two different high temperature anomalies. One is nearly rectangular in shape, residing above the core area of the identified geothermal prospect. The other appears to be in a narrow belt along the south and southeastern margin of Meager Creek, spatially coincident with a deep groundwater discharge zone along the margin of the MMVC (Fig. 7).

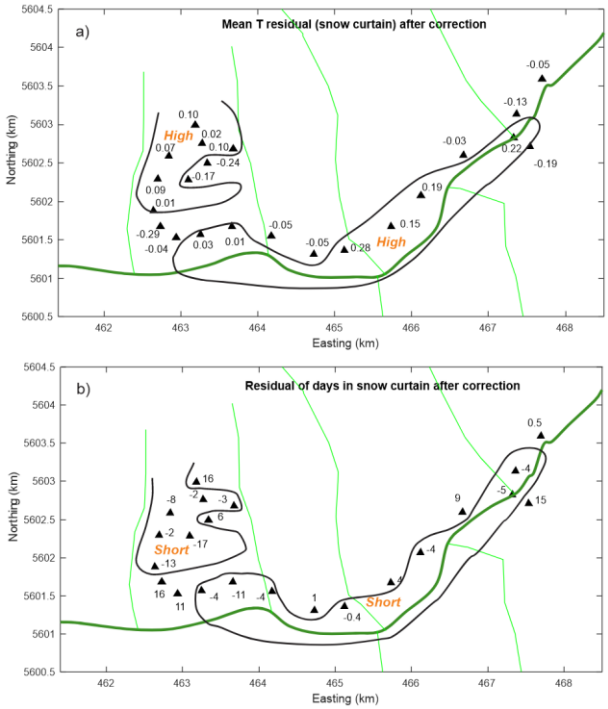

Figure 7: Map view of the residuals from the multivariate linear regression models, mean GST in SC period a), and days in SC period b) in the study area.

4 DISCUSSIONS

4.1 Subsurface temperature and heat flow mapping

Early geothermal exploration had drilled more than 20 slim temperature wells to determine subsurface temperature and delineate the geothermal prospect. The temperature profile of the wells shows two distinct geothermal regimes: a conductive dominating background with temperature gradient of 54 °C/km and heat flow <100 mWm^{-2}, and a convective heat flow disturbed high heat flow geothermal regime with temperature gradient of >500 °C/km and heat flow >1000 mWm^{-2} (Fig. 8a). Subsurface heat flow estimates from several authors (Lewis and Souther, 1987, Fairbank, et al., 1981, Reader, 1983 and Lewis et al. 1985) are compiled and mapped to outline their spatial variation (Fig. 9). The subsurface heat flow estimates from temperature wells and the occurrence of known surface warm/hot spring swarms (e.g., the Meager Creek hot springs) along the south and southeast bank of the Meager Creek suggest two heat flow anomalous zones, one in the core area of the identified geothermal prospect, and the other of deep groundwater discharge zone along the margin of the MMVC. The spatial accordance of the temperature anomalies from the mean GST (SC) and number of days (SC) with the subsurface geothermal anomalies may suggest some intrinsic relationship between the temperature anomalies from different indicators.

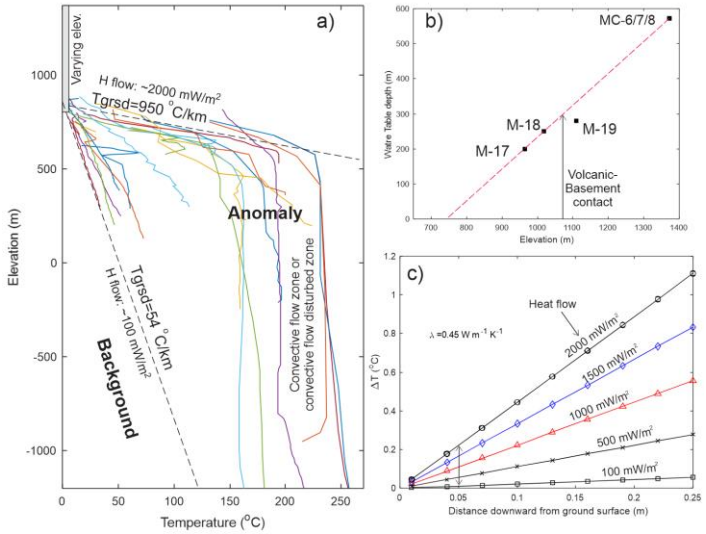

Figure 8: Geothermal regimes of the study area defined by subsurface temperature profiles of the geothermal exploration wells a); Water table depth interpreted from pressure data of the shallow exploration wells as a function of elevation b); and hypothesis test plot for the magnitude in ΔT due to subsurface heat flow contrasts for sensors between different burial depths, suggesting that large heat flow contrast between the background and anomaly zones is required to produce a ΔT of 0.2 °C in shallow depth (<5cm).

A close examination of the subsurface high temperature anomaly found that all stations from #1 to #8 are included in the core area delineated by previous exploration wells (Fig 9). There are 2 or 3 stations that are excluded in the depicted deep anomaly from GST monitoring data (Fig. 7a and b) when comparing with Fig 9. Chen et al. (2023) attributed this exclusion to environmental impacts. For mean GST (SC), Stations #4 and 5 are in the area underlain by volcanic rocks, close to the edge of the volcanic/basement boundary, where a high permeable volcanic deposit overlies impermeable basement diorite and discharge of cold ground water along the edge brought down the temperature. While #6 has a thin soil layer on an impermeable basement and high ground heat flow and latent heat dynamics at the contact between ground surface and base of snow cover resulted in high rate of downward cold-water drain, lowering the GST (SC). For the number of days (SC), Station #1 and 4 are not included in the detected anomaly. Station #1 is in northwest conner of the upper drilling pad, against two walls in the north and west topographically. High snow piles formed in the winter need more time to melt. Cold water discharge in the volcanic and basement contact boundary is considered to be the main reason for #4.

Although the difference in mean GST between the background and high GST anomalous areas is only less than 0.3 °C in the snow curtain period, to generate such a small difference in shallow depth requires a large contrast in geothermal heat flow. By assuming steady state heat flow during the SC period, the calculated GST difference from the theoretical model at shallow burial depth (<0.07 m) suggests that to generate GST difference of 0.25 °C, it requires significant heat flow contrast. For example, using a background heat flow of 100 mW m^{-2} and heat flow anomaly of 2000 mW m^{-2}, it yields GST contrast of 0.25 °C at a burial depth <0.05 m, which is consistent with the observed magnitude of GST difference between the anomalous area and background (Fig. 8b).

From the anomaly maps, it seems that there exists a nearly east-west low residual GST trend separating the two anomalies. This trend may represent a geological boundary that affects ground thermal fluid circulation, which is consistent with the AMT geophysical model.

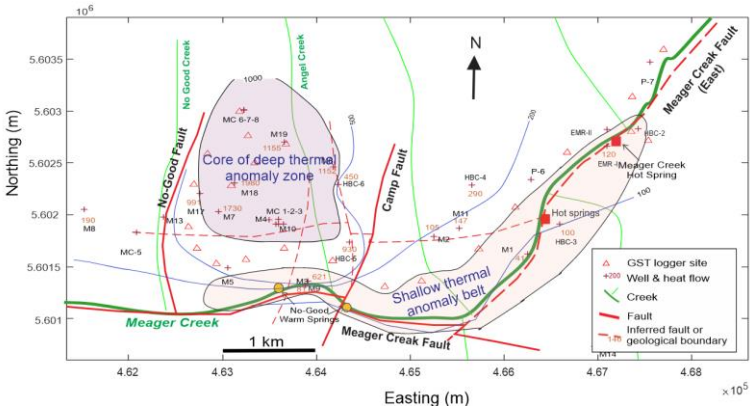

Figure 9: Background geology and heat flow map of the southern Meager geothermal prospective area. The heat flows were compiled from different sources (modified from Chen et al., 2023).

4.2 Geophysical signature of convective flow paths

A recent audio-magnetorelluric (AMT) survey was conducted and the data was inverted to a subsurface 3D electric resistivity model to reveal the conductive path for groundwater flow in southern Meager (Hormozzade Ghalati, et al. 2022). Their inverted 3D model suggested a complex subsurface resistivity structure in the southern Mount Meager Volcanic Complex. Although the meaning of the subsurface resistivity field is subject to geological interpretation, the modelled high conductive anomalies are spatially coincident with the known geothermal reservoir in fractured quartz diorite basement and near surface geothermal aquifers associated with the warm and hot springs, suggesting the geophysical model contains meaningful and interpretable information related to essential elements of a geothermal reservoir. Figure 10a is a horizontal slice of the inverted resistivity model of the AMT data at an elevation of 500 m (asl), showing two distinct low resistivity anomalies. The one, marked C1, is an elongated belt occurring along Meager Creek, spatially in accordance with the occurrence of hot-warm spring swarms along the margin of the volcanic complex. The other, marked C2, appears in a circular shape, coincident spatially with the core area of the known deep geothermal prospect. From a cross-section view along the W-E direction, the C2 low resistivity plunges to the west with a high angle and the anomaly extends down to more than -1000 m (bsl) in elevation (Fig. 12b). In contrast, the low resistivity anomaly C1 appears at a shallow depth in a tabular shape and remains with a relative stable thickness of about 600 m (Fig. 10c). In the north-south direction, C1 is restricted to the river valley. Whereas the upper boundary of the C2 anomaly mimics the topographic relief in general, but pierces high resistivity overburden at geological boundaries, such as between C1 and C2 and the contact between volcanic deposit and basement outcrop (Fig. 10d). Geological control of the deep resistive low is also obvious. For example, in the W-E direction, the C2 has sharp linear boundaries, sandwiched between the No Good fault and Angel fault (vent) (Fig, 10b). In the N-S direction, it appears to be a series of north dipping normal faults parallel to the Meager Creek Fault with the northmost fault zone (near M7 well) that separates the deep convective flow with the lateral flow in the shallow aquifer.

Clay-rich rock has low resistivity and is often used for interpreting observed low resistivities associated with mineral alteration in geothermal exploration (e.g., Spichak, et al., 2015). There are two slightly different resistivity models for geothermal interpretation. One believes that the low resistivity is a manifestation of the geothermal reservoir itself due to brine water in a fractured network, or porous media, while the other believes that the low-resistivity zone should be a clay alteration halo overlying or surrounding the high temperature reservoir (Spichak, et al., 2015). However, formation of a clay-rich interval in crystalline basement rock requires certain conditions, such as right temperature range, presence of movable water and certain types of minerals. Evidence shows that K-feldspar

grains can undergo a series of chemical reactions, including dissolution of feldspar and precipitation of kaolinite at shallow depth, and illilization at greater depth in sedimentary basins (Thyne et al., 2001). In volcanic settings, the clay-rich intervals are often associated with the moderate to strongly altered, pyritized and brecciated volcanics and crystalline intrusive rocks in fracture or fault zones (Fairbank engineering ltd., 2002). In cores from the temperature wells, Fairbank et al. (Fairbank engineering ltd, 2002) noticed that M19 well shows more evidence of fracture permeability and clay-rich intervals than either M17 or M18. Increased fracture permeability in M18 might be related to its closer proximity to the explosive volcanic vent in the Angel Creek drainage. Fracture permeability may be significant relation to the higher down-hole temperatures recorded at M19, which means high convective flow rate in high permeable fracture network. One interesting observation is that there is abundant pyrite in the altered rocks. Pyrite is more conductive than clay minerals and could be one of the reasons causing the fault bounded low resistivity anomalies, which is consistent with the AMT resistivity model (Figs. 10b and d).

Regional geological studies in western Turkey and the western Great Basin of the United States shown that many geothermal fields are associated with fault systems (e.g., Faulds, 2010). Hanano (2000) recognized the role of fractures in convective flow path development and geothermal reservoir formation. The two with contrasting economic significances differ at the scales and number of fractures involved in geological processes. Those are consistent with the observations of fault bounded anomalies in the 3D resistivity model and subsurface temperature anomalies in fractured diorite reservoirs from exploration drilling in the study area, suggesting deep circulated water saturated permeable fault and fracture networks could be the primary cause of low resistivity anomalies in this area.

The other interesting observation is the variable water table in the study area (Fig. 8b). The shallow high resistivity zone could be linked to the air saturated volcanic deposits and overburden above and around the water table. The air and meteoric/fresh ground water saturated rock have high resistivities and water circulation involving higher TDS water bodies may appear as low resistivity zones. Although the true nature of the modelled subsurface resistivity variation is subject to interpretation, the spatial accordance of low conductivity anomalies with known subsurface temperature distribution and geological evidence suggests that AMT data contain information critical for geological interpretation. The similarity in map view between the identified GST and low resistivity anomalies may suggest that some intrinsic relationship and convective groundwater circulation through permeable networks could be the linkage.

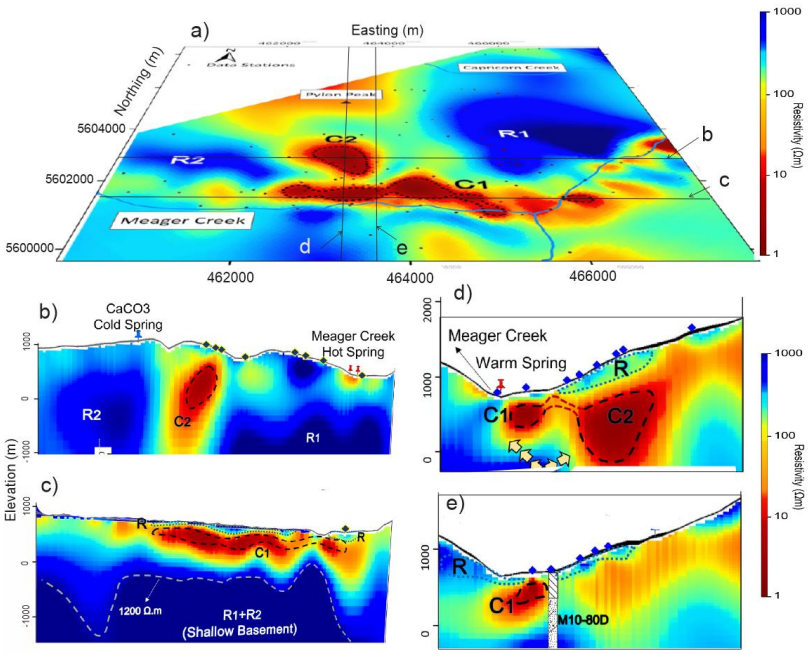

Figure 10. Inverted resistivity model from AMT data of the southern Mount Meager showing the subsurface rock resistivity structure (figure modified from Hormozzade Ghalati, et al. 2022). a) resistivity slice at 500 m elevation (asl) with locations of the four resistivity cross sections. Cross sections b) and c) in W-E direction, and d) and e) in N-S direction.

5 CONCLUSIONS

The study area has heterogeneous ground surface conditions. The collected GST time series are highly variable in space and time, a reflection of convoluted relationship among factors that influence the source, transmission, and storage of heat in soil. Due to predominance of solar heat flux, the GST monitoring data in snow free seasons show daily cycle and seasonal fluctuation and is further complicated by heterogeneous environmental conditions. The signal from geothermal heat flow is difficult to detect without rigorous modeling that considers all major physical processes and factors affecting the heat transmission.

In contrast, the solar radiation and weather forcing have been greatly suppressed in the snow curtain period, and the ground surface and near surface expression of subsurface heat flow and their spatial variation could be extractable from GST records. Statistical tools were used to eliminate the environmental impacts and to delineate GST anomalies that are potentially associated with subsurface heat flux. The subsurface temperature data from geothermal exploration wells, the inverted resistivity model from recent AMT model and

air infrared thermal images were used to constrain the GST data interpretation. The spatial coincidence between the indicators of high GST anomalies (mean GST and days in snow curtain period) and subsurface high heat flow zones may suggest an intrinsic linkage between the GST anomalies and areas of high subsurface heat flows. The inverted resistivity model from the AMT data seams to provide a visual connection between GST anomalies and subsurface heat flux variation through the interpretation of subsurface resistivity structure.

6 ACKNOWLEDGEMENTS

This represents an output from the Geoscience for New Energy Natural Program of Resources Canada. The Energy Research and Development Office of Natural Resource Canada and Geoscience BC provided financial support for the project. Prof. Glyn Williams-Jones, and his two students at Simon Frasor University helped deploy the temperature loggers in southern Meager area in 2020 field season.

7 REFERENCES

Chen, Z., Grasby, S., Yuan, W. and Liu X., 2023. Ground surface temperature monitoring data analysis and applications to geothermal exploration in volcanic areas, Mount Meager, western Canada, Geothermics 108 (2023) 102610, https://doi.org/10.1016/j.geothermics.2022.102610.

Davis J.: Statistics and Data Analysis in Geology, 3rd edn. John Wiley and Sons Inc., 2002. New York, p. 656. ISBN: 978-0-471-17275-8.

Fairbank BD; Openshaw; R. E. Souther, J. G. and Stauder, J, J., 1981a, Meager Creek geothermal project: an exploration case study, Geothermal Resources Council Bulletin July 1981, p3-7.

Fairbank engineering ltd, 2001-2002 drilling program south meager geothermal project British Columbia, 2002.

Faulds, J., Coolbaugh, M., Bouchot, V. Moeck, I. and Oğuz, K.: Characterizing Structural Controls of Geothermal Reservoirs in the Great Basin, USA, and Western Turkey: Developing Successful Exploration Strategies in Extended Terranes, Proceedings World Geothermal Congress 2010. Bali, Indonesia, 25-29 April 2010.

GeothermEx Inc., Report on the south meager geothermal resource British Columbia, Canada, for Western Geopower Corp. 156p. 2004.

GeothermEx Inc., Report on the south meager geothermal resource British Columbia, Canada, for Western Geopower Corp. 20p. 2009.

Hanano, M.: Two Different Roles of Fractures in Geothermal Development. Proceedings World Geothermal Congress 2000. Kyushu - Tohoku, Japan, May 28 - June 10, 2000. P. 2597-2562.

Hormozzade Ghalati, F., Craven, J. A., Motazedian, D., Grasby, S. E., Tschirhart, V. Modeling a Fractured Geothermal Reservoir Using 3-D AMT Data Inversion: Insights from Garibaldi Volcanic Belt, British Columbia, Canada. Geothermics. 105 (2022) 102526.

Lewis, T.J. and Souther, J.G.: Meager Mt., B.C.-Possible Geothermal Energy Resource: EMR, Earth Physics Branch, Geothermal Series No. 9 (1978), Ottawa, 17 pp.

Lewis,T.J, Jessop AM, and Judge, AS.: Heat flux measurements in southwestern British Columbia: the thermal consequences of plate tectonics. Canadian Journal of Earth Science, Vol. 22, 1985, p.1262-1273.

Reader, J.F.: Report to BC Hydro and Power Authority on Thermal conductivity and heat flow in diamond drill holes, Meager Creek geothermal area, southwestern British Columbia. 1983.

Stewart, ML.: Dacite block and ash avalanche hazards in mountainous terrain: 2360 yr. B.P. eruption of Mount Meager, British Columbia. M.Sc. Thesis, 2002.The University of British Columbia. https://open.library.ubc.ca/media/stream/pdf/831/1.0052463/1

Thyne, G., Boudreau, BP, Ramm, M and Midtbø, RE.: Simulation of potassium feldspar dissolution and illitization in the Statfjord Formation, North Sea. AAPG Bulletin, v. 85, no. 4 (April 2001), pp. 621–635.

Spichak, V.V., and Zakharova, O.K.: Chapter 1 - electromagnetic sounding of geothermal areas, in Viacheslav V., Spichak and Olga K. Zakharova, Electromagnetic Geothermometry, (2015), Pages 3-35. Elsevier.